


Article

# A Comparative Study on the Direct and Pulsed Current Electrodeposition of Cobalt-Substituted Hydroxyapatite for Magnetic Resonance Imaging Application

Wei-Chun Lin <sup>1</sup> , Chun-Chao Chuang <sup>2,3</sup>, Pin-Ting Wang <sup>1</sup> and Cheng-Ming Tang <sup>1,3,\*</sup>

<sup>1</sup> Institute of Oral Science, Chung Shan Medical University, Taichung 40201, Taiwan; tukust94114wenny@gmail.com (W.-C.L.); she07866@gmail.com (P.-T.W.)

<sup>2</sup> Department of Medical Imaging and Radiological Sciences, Chung Shan Medical University, Taichung 40201, Taiwan; jimchao@csmu.edu.tw

<sup>3</sup> Chung Shan Medical University Hospital, Taichung 40201, Taiwan

\* Correspondence: ranger@csmu.edu.tw

Received: 16 November 2018; Accepted: 24 December 2018; Published: 31 December 2018



**Abstract:** Hydroxyapatite has excellent biocompatibility and osteo-conductivity and, as the main inorganic component of human bones and teeth, is commonly used for bone repair. Its original characteristics can be changed by metal ion substitution. Cobalt ions can act as hypoxia-inducible factors and accelerate bone repair. At the same time, cobalt has paramagnetic properties and is often used in the study of medical imaging and target drugs. Through the introduction of cobalt ions, the unique hydroxyapatite has better biological activity and positioning of medical images. Herein, cobalt-substituted hydroxyapatite (CoHA) was synthesized on the surface of a titanium plate by electrochemical deposition and changes in the power output mode to explore the impact on CoHA. Electrochemical deposition with a pulse current significantly improved the productivity and uniformity of CoHA on the surface of titanium. CoHA show paramagnetic characteristics by a superconducting quantum interference device (SQUID). Resulting smaller particle size and circular morphology improves the magnetic strength of CoHA. Magnetic resonance imaging (MRI) of CoHA showed significant image contrast effect at low concentrations. The calculated particle relaxation rate was higher than other common MRI contrast agents. Biocompatibility of CoHA powder was evaluated using the human osteosarcoma cell line (MG63) which confirmed that CoHA is not cytotoxic and can promote cell growth and extracellular matrix mineralization. With the release of cobalt ions, CoHA was found to be significantly good in repression *E. coli* indicating about than 95% reduction in bacterial growth. The as-synthesized CoHA has a low degree of crystallinity, highly sensitive image contrast effect, and good bioactivity, and may have potential applications in bone repair and MRI.

**Keywords:** cobalt-substituted hydroxyapatite; pulsed electrode position; magnetic resonance imaging; antibacterial; anti-inflammatory

## 1. Introduction

Patients with defects due to trauma or osteoporosis must rely on fillers to make repairs. Currently, autologous bone graft, allogeneic bone graft and xenograft are widely used in bone filler materials. However, an autologous bone graft is limited by the disease incidence of donor and donor sites [1] and may incur high costs due to development of complications [2]. Allogeneic bone grafts and xenografts might lead to immune rejection and infectious diseases [3]. Therefore, many recent studies have

focused on the development of calcium phosphate bone graft material [4,5]. Hydroxyapatite (HA) is the common form of calcium phosphate bone graft [6]. HA is the main inorganic component of bones and teeth of vertebrates. Based on the stability and flexibility of the HA crystal structure, calcium ions on HA can be replaced with divalent metal cation such as iron [7], magnesium [8], silver [9], cobalt [10] etc. Due to cobalt ion being a hypoxia-mimicking agent, it can activate the hypoxia inducible factor-1 (HIF-1 $\alpha$ ) in mesenchymal stem cells and subsequently activate HIF-1 $\alpha$  target genes including vascular endothelial growth factor (VEGF) erythropoietin (EPO) [11–14]. Previous literature showed that cobalt substituted hydroxyapatite (CoHA) designed on the nano-scale can enhance osteogenesis in vivo [15]. Cobalt-substituted hydroxyapatite has paramagnetic properties [16] and can be developed as a contrast agent in magnetic resonance imaging (MRI) [17]. The superior contrast agents must have low toxicity, excellent chemical stability, high magnetic moment and ability to bind ligands to particles [18]. The application of CoHA should reduce the negative effects of currently used contrast agents on the human body. Traditionally, hydroxyapatite can be synthesized by many methods such as hydrothermal [19–21], wet precipitation [7,8,10,22] and electrochemical deposition [23–31]. In particular, electrochemical deposition can be achieved at lower working temperature and using simpler equipment than other methods. On the other hand, the HA coating by electrochemical deposition formed is more uniform [32] and has higher bond strength [15]. In our previous study, CoHA was successfully synthesized by electrochemical deposition procedure [33]. Electrochemical deposition can be divided into direct current (DC) power supply and pulsed current (PC) power supply according to the current supply mode. During the reaction, the instantaneous energy associated with a pulse current is higher than that of a direct current, leading to a reduction of metal ions at an extremely high over-potential. When the current is turned off, the discharge ion concentration near the cathode is restored to its initial value and concentration polarization disappears. This phenomenon for the next pulse cycle is conducive to the deposition of the surface. The purpose of this study is to synthesize CoHA via electrochemical deposition. Using the pulse current supply mode, the ion concentration near the cathode recovered its equilibrium value when the current was turned off, thus facilitating adsorption and generate of HA. The effects of different current supply modes on the morphology, magnetic properties and biodegradability were also compared in this study. The bioactivity of the CoHA powder was evaluated by examining the behavior of osteoblasts using MTT (3-(4,5-Dimethylthiazol-2-yl)-2,5-diphenyltetrazolium bromide) and Alizarin Red S assays. An evaluation of the antibacterial effects of CoHA using *E. coli* was carried out. Ultimately, this study aims to optimize CoHA production, to promote the repair of bone defects through release of cobalt ions and to provide marking and tracking in clinical MRI images.

## 2. Materials and Methods

### 2.1. Synthesis of Cobalt-Substituted Hydroxyapatite by Electrochemical Deposition

A commercial titanium sheet (99.9%, Opetech materials, Hsinchu, Taiwan) and 304 stainless-steel plate (Extra pure, Taichung, Taiwan) was cut into 80 mm  $\times$  40 mm  $\times$  1 mm. The samples were washed with acetone, ethanol and deionized water for 10 min using an ultrasonic shaker and removed at room temperature to dry. The electrolytic solution used 42 mM calcium nitrate (Shimada chemical works, Tokyo, Japan) and 25 mM ammonium dihydrogen phosphate (Showa chemical industry, Tokyo, Japan) in deionized water [34]. The pH of the electrolyte was adjusted at 3.52 using hydrochloric acid and tris(hydroxymethyl)aminomethane (Tris). Finally, 7.9 mM Cobalt chloride (Shimada chemical works, Tokyo, Japan) was added and stirred until it completely dissolved. Titanium piece as a cathode, 304 stainless steel plate as an anode. Were used direct current (DC) and pulse current (PC) for electrochemical deposition (Figure 1). The temperature of the electrolyte solution was controlled at 55 °C and the voltage was 5.5 V for electrochemical deposition. There are three groups in this experiment, for the DC-CoHA (DC-type electrode position), PC<sub>1</sub>-CoHA (pulsed electrode position same time as the DC), and the PC<sub>2</sub>-CoHA (pulsed electrode position with the same power as the DC),

respectively (Table 1). After deposition, CoHA was cleaned using deionized water and dried at room temperature. Finally, the powder on the titanium piece was scraped off to acquire the CoHA particles.

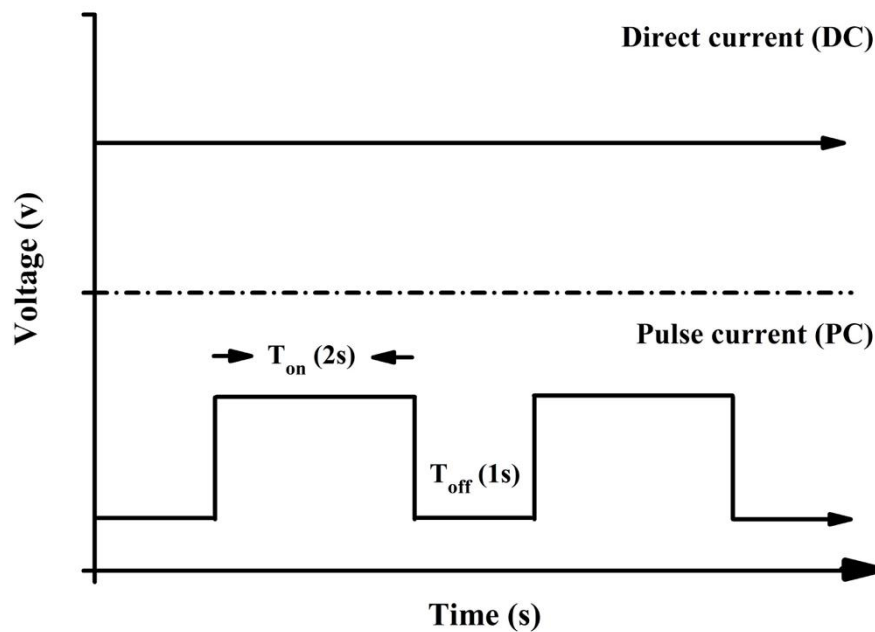


Figure 1. Schematic diagram of direct current and pulse current supply.

Table 1. The particles size and magnetism parameters ( $H_c$ ,  $M_s$  and  $M_r$ ) of CoHA.

Sample	Particle Size			Magnetism Parameters		
	Length (nm)	Width (nm)	Aspect Ratio	$H_c$ (Oe)	$M_s$ (emu/g)	$H_r$ (emu/g)
DC-CoHA	$365 \pm 11$	$285 \pm 80$	1.28	261.41	0.86	0.26
PC <sub>1</sub> -CoHA	$418 \pm 80$	$370 \pm 90$	1.13	133.73	0.79	0.15
PC <sub>2</sub> -CoHA	$602 \pm 73$	$510 \pm 67$	1.18	132.18	0.65	0.09

## 2.2. Surface Characterization

The microstructures of the surface of the powder were observed by a field-emission scanning electron microscope (FE-SEM) (JSM-7610F, JEOL, Tokyo, Japan). Element composition on the powders surface was measured by energy-dispersive X-ray spectroscopy (EDS, JEOL, Tokyo, Japan). The Fourier transform infrared spectrometer (FTIR) (Vertex80v, Bruker, Billerica, MA, USA) was used to study the surface functional groups of materials. The scanning range of this study is  $400\text{--}4000\text{ cm}^{-1}$  and the number of scans is 200 times. The phase composition of the CoHA powders was determined by X-ray diffractometer (XRD) (Miniflex II, Rigaku, Tokyo, Japan) using  $\text{CuK}\alpha$  radiation ( $\lambda = 1.54\text{ \AA}$ ). The scanning conditions for this study were  $4^\circ/\text{min}$  and the scanning range was  $10^\circ\text{--}70^\circ$ . The crystal size of hydroxyapatite is calculated by the following formula,  $X_s = 0.9\lambda/\text{FWHM} \times \cos\theta$ ,  $X_s$  is the grain size (nm),  $\lambda$  is the  $\text{CuK}\alpha$  radiation, FWHM (full width at half maximum) is the half width of the diffraction peak,  $\theta$  for the diffraction peak angle. The crystallinity of hydroxyapatite is calculated by the following formula:  $X_c = (K/\beta)^3$ ;  $K$  is a constant of 0.24 [35].

## 2.3. Internal Ion Composition

Determination of the overall elemental composition in the CoHA was undertaken by inductively coupled plasma optical emission spectrometry (ICP-OES) (Optima 8300, Perkin Elmer, Waltham, MA, USA). The amount of powder was weighed, 1 mL of 65% nitric acid was added so that the sample

completely dissolved, and then it was filtered through 0.45 µm filter and the concentration range and dilution of the calibration line was set.

#### 2.4. Magnetic Analysis

Magnetic properties of CoHA was obtained using superconducting quantum interference devices magnetometer (SQUID) (MPMS5, Quantum Design, San Diego, CA, USA) in an applied magnetic field of  $-10,000$  Oe to  $10,000$  Oe at  $37$  °C.

#### 2.5. In Vitro Biodegradation

Each sample take  $0.1$  g was immersed in  $10$  mL of phosphate buffered saline (PBS), placed in a constant temperature water bath and the temperature was maintained at  $37$  °C for four weeks and the pH was measured daily. The PBS composition has KCL,  $\text{KH}_2\text{PO}_4$ , NaCl and  $\text{Na}_2\text{HPO}_4$ . The samples were soaked for 7 days and the release of ions was measured by ICP-OES.

#### 2.6. Free Radical Scavenging Effects

The free radical scavenging activity was evaluated using 2,2-diphenyl-1-picrylhydrazyl (DPPH) free radical [36,37]. One mL of distilled water (as control group) or 1 mL of deionized water containing  $0.01$  g CoHA, was added to 3 mL of  $32\text{-}\mu\text{M}$  DPPH free radical in methanol and left to stand for 90 min at room temperature. Absorbance of the reaction mixture was then measured at  $517$  nm using an ultraviolet–visible spectrophotometer (UV/VIS) (Helios Zeta, Thermo, Waltham, MA, USA). The free radical scavenging effect is determined by the following equation: scavenging ratio (%) =  $[1 - (\text{absorbance of test sample}/\text{absorbance of control})] \times 100\%$ .

#### 2.7. In Vitro Magnetic Resonance Imaging (MRI) Examination

MRI tests were performed on a  $1.5$  T MRI scanner (Signa Horizon LX, GE Healthcare, Chicago, IL, USA). A certain amount of HA and CoHA powders were dispersed in a gelatin (Sigma Aldrich, St. Louis, MO, USA) with different concentrations and then poured into  $5$  mL distilled water. The sample and gelatin solution were mixed thoroughly while at  $70$  °C. The gelatin mixture was allowed to cool to room temperature. The  $T_1$ -weighted images were acquired using spin echo imaging sequencing with the following parameters: matrix size =  $256 \times 256$ , field of view =  $180$  mm  $\times$   $180$  mm, slice thickness =  $5$  mm, echo time =  $26$  ms, repetition time =  $100$  ms, number of acquisitions =  $2$ . Color image processing was performed using ImageJ (1.51K, National Institutes of Health, Bethesda, MD, USA). The contrast-enhancing efficacy of CoHA and commercial HA were determined by its relaxation coefficient ( $r_2$ ). The  $r_2$  is calculated by the following formula (Equation (1)) [38]:

$$\frac{1}{T_2} = \frac{1}{T_2^0} + r_2C \quad (1)$$

where  $T_2$  is the observed relaxation time in the presence of CoHA,  $T_2^0$  is the relaxation rate of pure gelatin and  $C$  is the concentration of cobalt ion.

#### 2.8. Biocompatibility

We used a mouse-derived established cell line (L929) of fibroblasts and human osteosarcoma cell line (MG63), maintained in Dulbecco's modified eagle medium (DMEM) supplemented with 10% fetal bovine serum (FBS) (Biological Industries, Cromwell, CT, USA) at  $37$  °C in a 5%  $\text{CO}_2$  incubator (310, Thermo Fisher Scientific, Waltham, MA, USA) in this study in order to investigate the effect of ions released by CoHA on cells. We used the CoHA extract for testing. Using  $0.1$  g of three CoHA powders each immersed in  $1$  mL of deionized water and soaked for 7 days at  $37$  °C. Moreover, we used cobalt ion standard solution (AccuStandard, New Haven, CT, USA), diluted to  $1$  and  $10$  ppm, as a positive control followed by centrifugation, aspiration of the supernatant, and removal of the liquid using a

freeze dryer (FDU-1200, Tokyo Rikakikai, Tokyo, Japan). Then 10 mL of DMEM was added to each sample and filter with a 0.22  $\mu\text{m}$  sterile filtration apparatus as a culture medium for cell test. L929 and MG63 cells were seeded in 24 well at  $5 \times 10^4$  cells/well, cultured for 18 h and replaced with extract. Finally, it was cultured in a 37 °C, 5% CO<sub>2</sub> cell incubator for 24, 48 and 72 h. The biocompatibility was evaluated by the colorimetric MTT (3-(4,5-Dimethylthiazol-2-yl)-2,5-diphenyltetrazolium bromide, MTT) assay. The absorbance (O.D.) of the wavelength of 563–650 nm was read with an enzyme-linked immunosorbent assay (ELISA) reader (Sunrise, Tecan, Männedorf, Switzerland). The biocompatibility was expressed as the percentage of compared to that control tissue culture plate (TCP).

### 2.9. Extracellular Matrix Mineralization

Alizarin Red S (ARS) (Sigma Aldrich, St. Louis, MO, USA) is an orange-yellow needle-like crystal, alizarin sulfonate sodium salt. With calcium salt to chelate the formation of orange-red deposition complex, the detection of calcium deposition in cultured cells. Using 2% ARS, pH between 4.1–4.3. MG63 cells ( $1 \times 10^4$  cells/well) were cultured with the extract for 3 and 7 days, then washed 2–3 times with PBS and fixed with 4% paraformaldehyde for 10 minutes. After removal, they were rinsed with deionized water once, add ARS, and reaction for 15 minutes at room temperature. Ultimately, deionized water was used to wash them 2–3 times. The results of staining were observed by optical microscope. In the quantitative analysis, the ARS on the specimen after washed with distilled water was dissolved in 0.2 M NaOH/methanol (1:1) to measure the optical density at 620 nm [12].

### 2.10. Antibacterial

The CoHA were investigated against *E. coli* as model Gram-negative bacteria by the colony plate count method in order to quantify the bacterial effect of our system. The *E. coli* were prepared from fresh brain heart infusion (BHI, Becton Drive, Franklin Lakes, NJ, USA) and incubated at 37 °C for 24 h. The BHI containing *E. coli* was diluted to  $10^{-3}$  of its original concentration, and 1 mL of bacteria liquid was extracted and added a fixed weight (6 mg) of CoHA samples, placed into a centrifuge tube and cultivated for 18 h. After the samples were removed, 100- $\mu\text{L}$  bacterial solution was extracted and applied on the BHI Agar (Becton, Dickinson and Company, Houston, TX, USA) petri dish before being cultured for 24 h at 37 °C. Finally, the colonies were counted, and the results were expressed as percentage reduction rates of bacteria number =  $[\alpha \times 10^5]$ , where  $\alpha$  is the number of bacterial colonies.

### 2.11. Statistical Analysis

All data from the average of the three repeat samples  $\pm$  standard deviation. Data were calculated using JMP14 software (JMP<sup>®</sup>14.1.0, Cary, NC, USA). One-way analysis of variance (ANOVA) was used to examine the differences between groups using the Tukey HSD multiple comparison.  $p < 0.05$  is considered to be significant.

## 3. Results and Discussion

### 3.1. Surface Characterization

The CoHA synthesized using different current supply modes were denoted as DC-CoHA, PC<sub>1</sub>-CoHA and PC<sub>2</sub>-CoHA. After cleaning and drying, the deposit appeared lilac in color due to the presence of cobalt ions (Figure 2). The distribution of apatite deposits was analyzed using imaging software (Image J), indicated by the red area observed in Figure 2A. The PC power supply produced better CoHA deposition on the cathode metal plate than DC, because the ions provided by the intermittent power supply mode when pulse current is applied reach an equilibrium content when the current is turned off. The surface morphology of CoHA was observed using FE-SEM (Figure 2B). All groups of CoHA particles were spherical and densely packed together. In 2014, Gopi et al. reported that the spherical morphology HA is conducive to cell attachment and proliferation [39]. Therefore, the shape of CoHA has a positive effect on cell growth. FE-SEM images were analyzed

using Image-Pro Plus software. The calculated particle size descended in the order: PC<sub>2</sub>-CoHA, PC<sub>1</sub>-CoHA and DC-CoHA (Table 2). The surface elemental composition of CoHA was analyzed using energy-dispersive X-ray spectroscopy (EDS). The DC-CoHA surface contained the highest amount of elemental cobalt (3.4 at %), followed by PC<sub>2</sub>-CoHA (2.9 at %) and PC<sub>1</sub>-CoHA (2.2 at %).

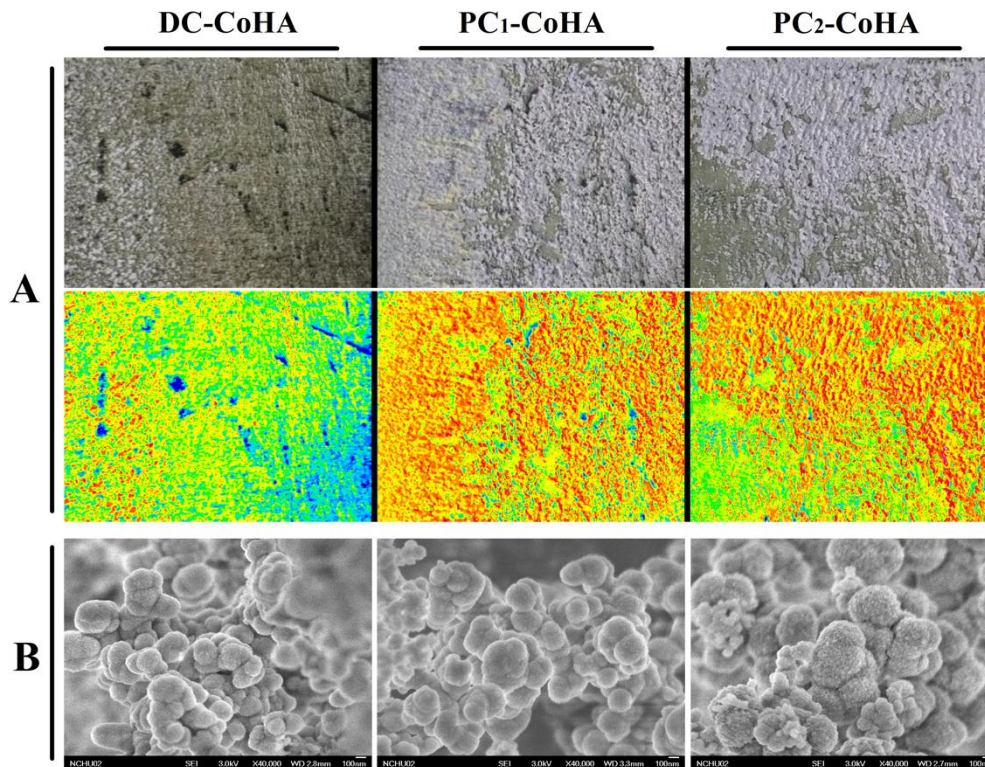


**Figure 2.** The surface morphology of the Co-HA particles was observed by (A) camera and (B) field-emission scanning electron microscope (FE-SEM). The color map is obtained using the surface image via Image J software analysis and red represents the distribution of Co-HA.

**Table 2.** The construct parameters of the as synthesized CoHA particles by X-ray diffraction (XRD) analysis.

Sample	2 $\theta$	Line Width (FWHM)	Crystallite Size X <sub>s</sub> (nm)	Fraction Crystallinity X <sub>c</sub>
DC-CoHA	25.87	0.77	1.849	0.030
PC <sub>1</sub> -CoHA	25.94	1.08	1.318	0.011
PC <sub>2</sub> -CoHA	25.92	0.91	1.565	0.018

The FTIR spectra of CoHA synthesized using different current modes are shown in Figure 3. The absorption peaks at wave numbers of 564.1 cm<sup>-1</sup>, 603.6 cm<sup>-1</sup>, and 1043 cm<sup>-1</sup> represent PO<sub>4</sub><sup>3-</sup>, while those at 1381.1 cm<sup>-1</sup> and 1647 cm<sup>-1</sup> represent C=O [40]. The peaks at 873.0 cm<sup>-1</sup>, 1423.3 cm<sup>-1</sup> and 1483 cm<sup>-1</sup> represent type B carbonate bands [41–43]. One study has indicated that CO<sub>3</sub><sup>2-</sup> can promote the degradation of HA, provides calcium and phosphorus ions. Which can be adsorbed during bone remodeling, thereby improving bone growth [44]. The peak at 3484 cm<sup>-1</sup>, representing OH<sup>-</sup>, are observed in three powder groups DC-CoHA, PC<sub>1</sub>-CoHA, and PC<sub>2</sub>-CoHA (Figure 3B), among which DC-CoHA showed the largest peak shift. This could be caused by the addition of CoCl<sub>2</sub>, which combined with OH<sup>-</sup> to observed peak shift. The HA component of the CoHA was confirmed via FTIR analysis [35,45].

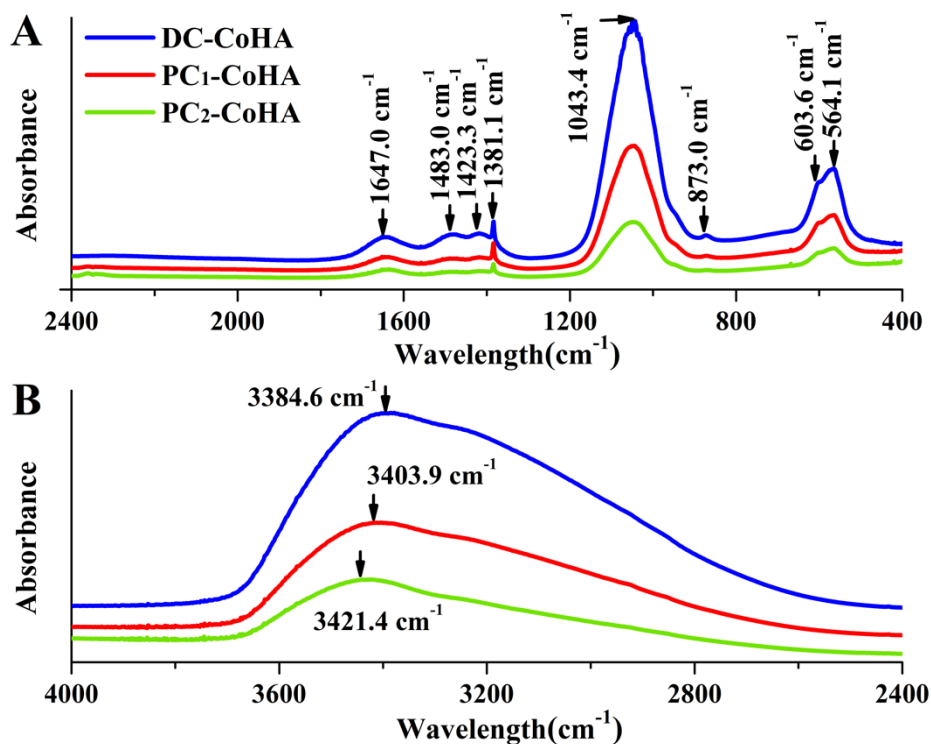


**Figure 3.** The attenuated total reflectance-Fourier transform infrared spectroscopy (ATR-FTIR) spectrum of the CoHA particles. (A) at 400–2400  $\text{cm}^{-1}$  range, (B) at 2400–4000  $\text{cm}^{-1}$  range.

The X-ray diffraction analysis results of the powder crystal structure is shown in Figure 4. These results were compared with literature; diffraction peaks of HA crystals were observed at  $26.01^\circ$  (002),  $32.04^\circ$  (211),  $39.68^\circ$  (310),  $46.81^\circ$  (222) and  $49.74^\circ$  (123) [46,47], and the diffraction peak of  $\text{Co}_3\text{O}_4$  was observed at  $18.8^\circ$  (111) [16,48], which confirmed the presence of the CoHA structure. Since none of the CoHA powder are calcined, all the samples belonged to the low crystallinity range. Despite this, the  $\text{PC}_1$ -CoHA and  $\text{PC}_2$ -CoHA samples showed larger half widths and lower peaks. The CoHA produced by the display of the pulse current supply mode has more structures that are amorphous. However, materials with high crystallinity cannot degrade easily, and in bone tissue engineering, accelerated degradation of HA is preferred during bone repair to facilitate the absorption of osteoblasts and rapid recovery of bone defects [49].

### 3.2. Internal Ion Composition

The results calculated based on inductively coupled plasma optical emission spectrometry (ICP-OES) analysis are shown in Table 3. After cobalt ion substitution, the Ca + Co/P ratio was calculated to be 1.67–1.72, similar to the Ca/P ratio of human bone (1.67). The cobalt ion contents for the three CoHA powder groups were 13–14%, slightly higher than the initial electrolyte concentration (10%). While DC-CoHA had the highest surface cobalt ion content according to the EDS surface elemental analysis, the ICP-OES analysis of three groups showed similar internal cobalt substitutions (14%). This indicates that CoHA synthesized using DC power supply has higher surface cobalt ion substitution, while PC power supply results in higher internal cobalt ion substitution.

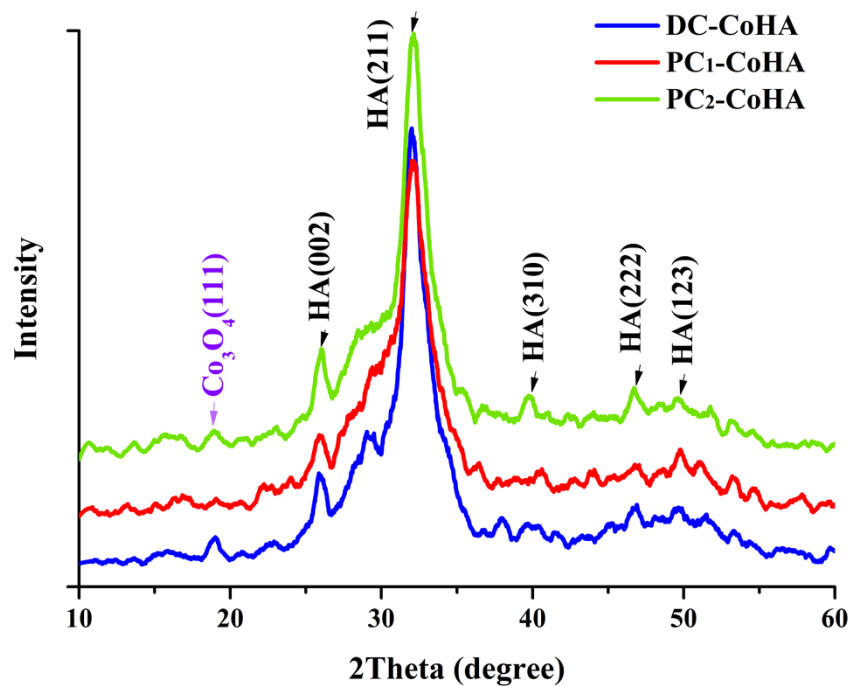


**Figure 4.** XRD patterns of the CoHA samples synthesized with different power supply.

**Table 3.** Element ratios inside CoHA particles and ion release concentration in CoHA immersed phosphate buffer solution by inductively coupled plasma optical emission spectrometry (ICP-OES).

Sample	Particle		Extraction Solution		
	Ca + Co/P	X <sub>co</sub> (%)	Ca (ppM)	Co (ppM)	P (ppM)
PBS	N.D.	N.D.	N.D.	N.D.	541
DC-CoHA	1.72	14.0	1.04	1.45	434
PC <sub>1</sub> -CoHA	1.67	14.0	1.68	1.86	429
PC <sub>2</sub> -CoHA	1.68	13.0	1.21	1.72	425

The extraction solution was obtained by immersing the powder in phosphate-buffered saline (PBS) at 37 °C for 7 days.

### 3.3. Magnetic Analysis

The hysteresis curve of CoHA was measured using a superconducting quantum interference magnetometer (Figure 5). According to literature, a negative slope indicates a diamagnetic hysteresis curve for pure HA [16]. In this study, a positive slope was observed for CoHA, corresponding to a paramagnetic hysteresis curve. Coercivity ( $H_c$ ), saturation magnetization ( $M_s$ ), and remanent magnetization ( $M_r$ ) were calculated from Figure 5 (Table 2). The results show that DC-CoHA has the highest magnetism, followed by PC<sub>1</sub>-CoHA and PC<sub>2</sub>-CoHA. The magnetic properties of a material can be affected by many factors, such as size, structure, surface morphology, crystallinity, and defects. The DC-CoHA surface contains relatively more cobalt ions and, therefore, has higher magnetism. On the other hand, the magnetic properties of PC<sub>1</sub>-CoHA and PC<sub>2</sub>-CoHA can be explained by their particle morphologies and sizes (Table 2). PC<sub>1</sub>-CoHA particle size is smaller than PC<sub>2</sub>-CoHA. Therefore, these two powder groups showed different levels of magnetism. The results are similar to that reported in literature, i.e., smaller particles have higher magnetism [38,50]. In 2014, Kramer et al. [10] synthesized CoHA powder using ion exchange and wet methods. Their magnetic analysis results showed that the  $M_s$  of CoHA synthesized by ion exchange and wet methods were 0.2 emu/g and 0.1 emu/g, respectively. In 2015, Sarath Chandra et al. [16] reported that CoHA synthesized by combining hydrothermal and microwave irradiation techniques had an  $M_s$  value of up to 0.06 emu/g. Compared to other synthesis methods, the CoHA synthesized via electrochemical deposition



had significantly higher magnetism, with the highest  $M_s$  value detected herein being 0.9 emu/g. The SQUID results confirmed the substitution of a small number of cobalt ions in the HA lattice, resulting in the generation of a paramagnetic material. In addition, the low crystallinity of the three kinds of CoHAs in this study belongs to amorphous materials. Most amorphous materials show that hysteresis is unusual. However, Erica Kramer et al. used ion exchange and wet synthesis to synthesize CoHA. The authors point out that the two CoHAs have very low crystallinity due to the addition of Co, and it shows that they belong to the amorphous material [10]. However, the results of the magnetic analysis showed that the magnetization of CoHA showed a positive slope indicating a paramagnetic property. Therefore, although the crystallinity of the material is very low in this study, CoHA is superparamagnetic due to the presence of cobalt ions.

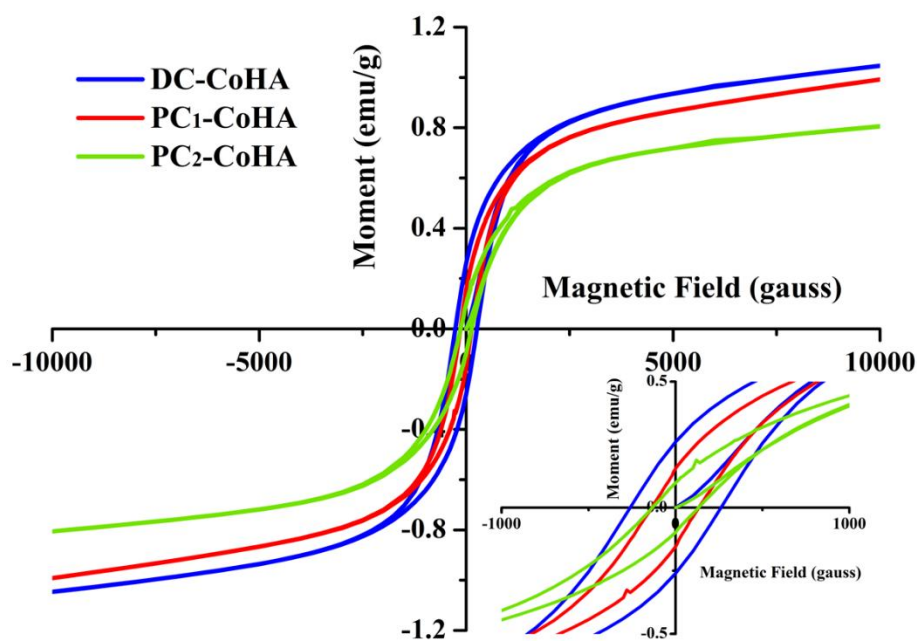


**Figure 5.** Mass magnetization measurements of Co-HA sample by superconducting quantum interference device (SQUID).

#### 3.4. In Vitro Biodegradation

To simulate the environment in the human body, samples were soaked in PBS at 37 °C for four weeks. The results of a short-term dissolution test in Figure 6A showed that when three kinds of CoHA were immersed to the PBS, respectively, the anion and cation will be released in the initial period. However, anion (phosphorus) is released faster than cation (calcium, cobalt) lead to increase of pH value. Then, cation release slows down the increase of pH value. This tendency is consistent with the literature [10], slow dissolution of hydroxyapatite and increase of hydroxy group in solution leads to an increase of pH value. Consequently, when the pH value changes, it means that there are more calcium and cobalt ions released. Therefore, CoHA prepared by the PC method can obtain a good degradation effect compared with the DC method. In particular, PC1-CoHA has a significant difference at 24 h. In addition, the pH rises a lot before 24 h, followed by a slow rise and remaining at 8.97 after day 15. The originally neutral PBS solutions for all the groups turned alkaline after four weeks of soaking due to the dissociation that occurred after soaking. The results of CoHA powder after soaking in PBS for seven days are shown in Table 3. The release concentration of cobalt ions was 1.45–1.86 ppm. The release of cobalt ions from PC<sub>1</sub>-CoHA and PC<sub>2</sub>-CoHA is higher than DC-CoHA, thus affecting the pH bias towards neutrality. Due to low crystallinity, the PC<sub>1</sub>-CoHA powder degraded faster. Therefore, CoHA prepared by the PC method can obtain a good degradation effect compared with the DC method. In particular, PC<sub>1</sub>-CoHA has a significant difference at 24 h. At the same time, the literature points

out that increasing the concentration of calcium and phosphate ions in the bone defect can effectively promote the growth of bone [51,52].

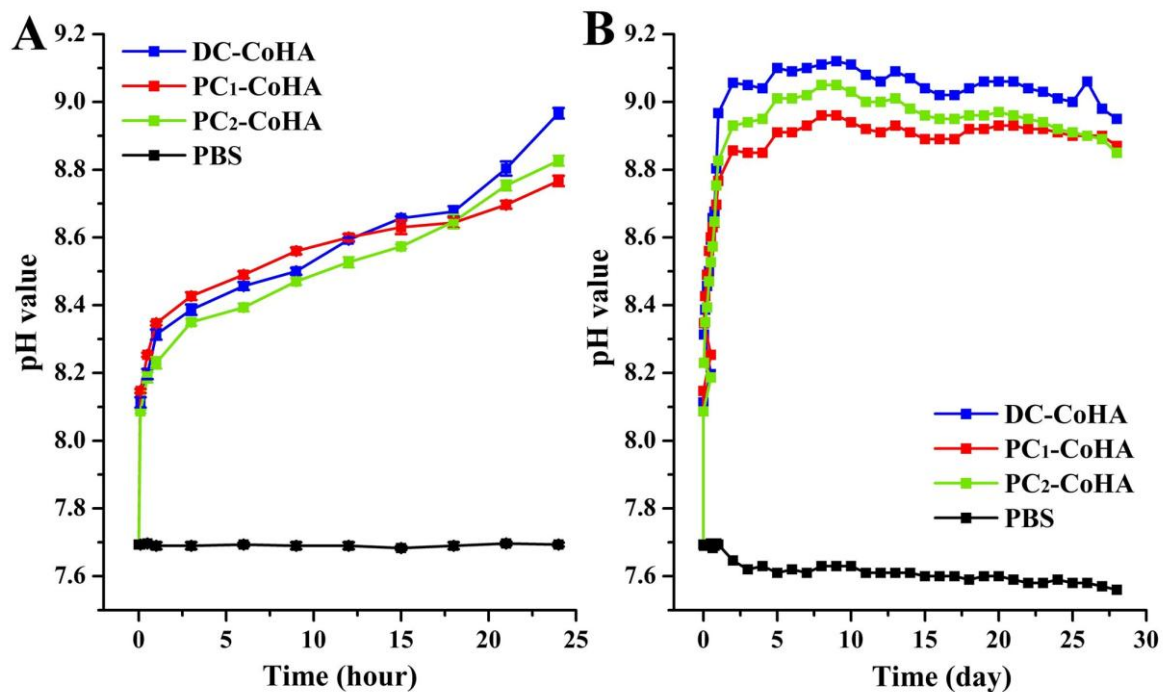


Figure 6. The pH values of different CoHA particles soaked in PBS solution at (A) 24 h and (B) 4 weeks.

### 3.5. Free Radical Scavenging Effects

Figure 7 shows the rates of free radical scavenging. HA and cobalt standard solution were used as a control group. The results show that the free radical scavenging ratio of the three groups of CoHA samples mainly comes from cobalt ions. In particular, DC-CoHA had the highest free radical scavenging ratio of 50% among the samples, because the surface of DC-CoHA powder had more cobalt ions, allowing more combinations with free radicals. Free radicals are produced during biological differentiation and defense; however, too many free radicals may cause excessive oxidation. Antioxidants can be used to maintain the normal growth of organisms by capturing harmful free radicals; thus, they play an important role in this balance. A previous study showed that the anti-oxidative properties of Ag nanoparticles in waterborne polyurethanes can reduce both in vitro and in vivo inflammations [53]. Therefore, the free radical scavenging capability of CoHA can induce anti-inflammatory effects in cells, reducing inflammatory reactions and promoting bone repair at defect sites.

### 3.6. In Vitro MRI Examination

Due to the structural differences of human tissues, the differences between tumor and normal tissue can be detected using MRI, and the location of therapeutic agents can also be tracked simultaneously. MRI has many advantages: it has extremely high imaging flexibility, does not have apparent detrimental effects on patients, enables the generation of high-resolution images with excellent contrast for different tissues, provides physiological parameters, and facilitates the acquisition of unique clinical information [54,55]. However, metal implants or fillers used for bone defects often interfere with clinical MRI imaging judgment due to the inherent characteristics of the materials [56]. A previous study, which used cobalt ferrite/graphene oxide nanocomposites (CoFe<sub>2</sub>O<sub>4</sub>/GO) as a carrier, showed a high MRI relaxation rate, indicating its great potential for application in clinical MRI [17]. In this study, commercial HA was used as the control group for the MRI test. To verify the diagnostic potential of CoHA, T<sub>2</sub>-weighted MRI images were obtained

at different sample concentrations at room temperature (Figure 8). Figure 8A shows that the signal intensity of the MRI image increases with increasing concentration of cobalt ions, and a clear boundary is also shown in the image. However, no significant changes are observed in the image for pure HA. Figure 8B shows the results of the relaxation rate,  $R_2$  ( $1/T_2$ ). A linear increase was observed for all samples, indicating the generation of a  $T_2$ -weighted spin-echo sequence in the MRI of CoHA. The higher values of  $R_2$  achieved a greater contrast effect. The relaxation rates ( $r_2$ ) is obtained from the curve of  $R_2$  versus, and is a standardized contrast enhancement index [57]. The CoHA  $r_2$  measured for different cobalt ion concentrations are shown in Figure 8C. DC-CoHA has the highest relaxation rate  $283.4 \text{ mM}^{-1}\text{s}^{-1}$ , followed by  $\text{PC}_1$ -CoHA ( $227.8 \text{ mM}^{-1}\text{s}^{-1}$ ) and  $\text{PC}_2$ -CoHA ( $223.3 \text{ mM}^{-1}\text{s}^{-1}$ ). Although CoHA synthesized using pulse current has a lower relaxation rate than that using direct current, the  $r_2$  was still significantly higher than the contrast agent ferrite ethanol ( $91 \text{ mM}^{-1}\text{s}^{-1}$ ) [38] and other cobalt-containing nanoparticles [17,58,59]. MRI contrast agents with high  $r_2$  can drastically shorten the  $T_2$  relaxation time at relatively low concentrations [38,58]. Since the surface of DC-CoHA may be attached with more cobalt ions (with unpaired electrons, it is easy to disturb the magnetic field), this produces higher magnetic properties ( $M_s$ ), resulting in higher relaxation rates ( $r_2$ ) than  $\text{PC}_1$ -CoHA and  $\text{PC}_2$ -CoHA (Figure 8C). At the same time, together with the literature, the results show that the relaxation rate  $r_2$  is proportional to the saturation magnetization [38,60]. Therefore, DC-CoHA has a higher relaxivity  $r_2$ . The MRI test confirmed that CoHA had relatively high relaxation rates at low concentrations, allowing it to be used for localization in  $T_2$  imaging applications like MRI markers (gold seeds) [61–63]. In future, CoHA may be used as a filler for bone defects, and clinicians may be able to determine the progress of bone tissue repair and track the location of CoHA using MRI.

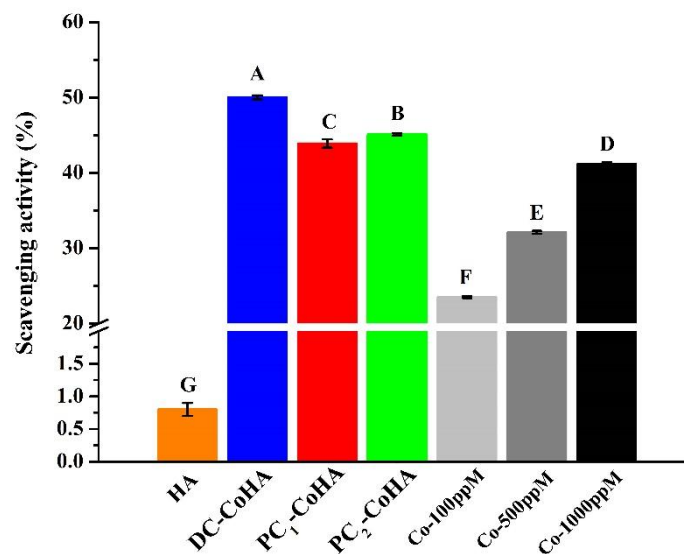
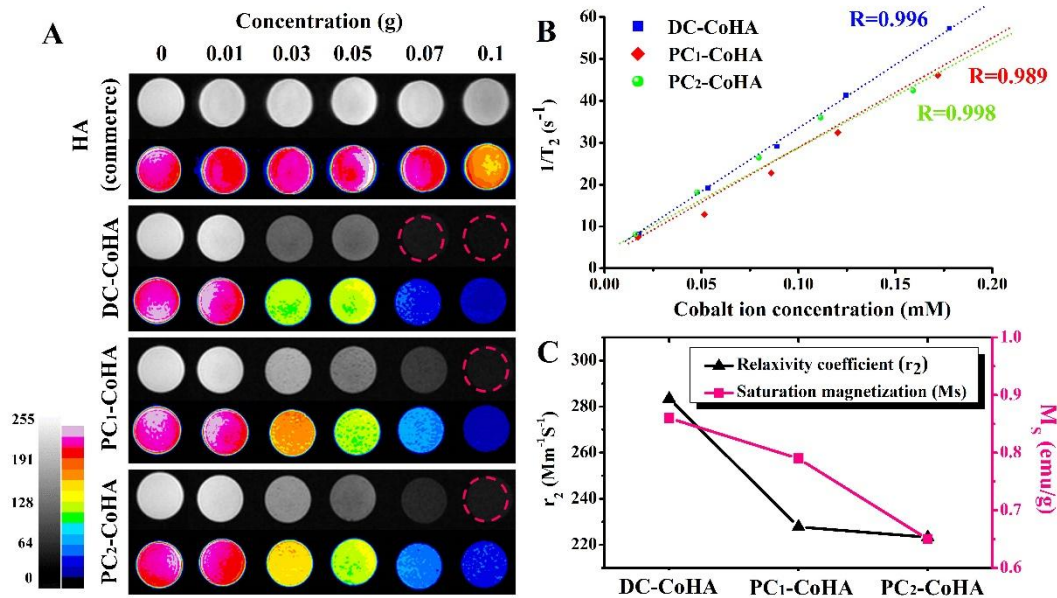


Figure 7. Free scavenging ratios of CoHA particles ( $p < 0.05$ ).

### 3.7. Biocompatibility

The L929 and MG63 cell lines were cultured in the CoHA extract solutions. The MTT assay was used to evaluate the biocompatibility at different time intervals (Figure 9). A tissue culture plate (TCP) was used as the control group. After culturing the L929 cell line for 72 h, no significant differences were observed when comparing the three CoHA groups with 1 ppm cobalt ions and the TCP. However, a sharp drop in cell viability was observed when the cobalt ion concentration was increased to 10 ppm. During the initial period of MG63 culture (24 h), a significant improvement in cell viability was observed for  $\text{PC}_2$ -CoHA and the 1-ppm cobalt ion groups. After 72 h of culture, cell viability for  $\text{PC}_1$ -CoHA was significantly higher than the other groups, and was 16% higher than the TCP control group.  $\text{PC}_2$ -CoHA also had significantly higher cell viability than the control group. The two cell lines show that cobalt ions did not significantly promote proliferation of fibroblasts, whereas the

proliferation of human osteosarcoma cells was significantly improved at a cobalt ion concentration of 1–2 ppm. Cell viability decreased when the cobalt ion concentration was increased to 10 ppm. These observations indicated that CoHA synthesized using both DC and PC power supplies had no obvious cytotoxicity, and PC<sub>1</sub>-CoHA significantly improved bone cell growth. Moreover, HA shows that the release of calcium and phosphorus ions contributes to cell growth. However, in the three sets of CoHA samples, a small number of cobalt ions added would give better cell growth than pure HA.



**Figure 8.** (A) T<sub>2</sub>-weighted magnetic resonance imaging (MRI) images of hydroxyapatite (HA) (commerce), DC-CoHA, PC<sub>1</sub>-CoHA and PC<sub>2</sub>-CoHA suspended in gelatin at different concentrations; (B) the T<sub>2</sub> relaxation rate R<sub>2</sub> (1/T<sub>2</sub>) against cobalt concentration of CoHA; (C) relaxivity coefficient (r<sub>2</sub>) and saturation magnetization (M<sub>s</sub>) of the relative relationship.

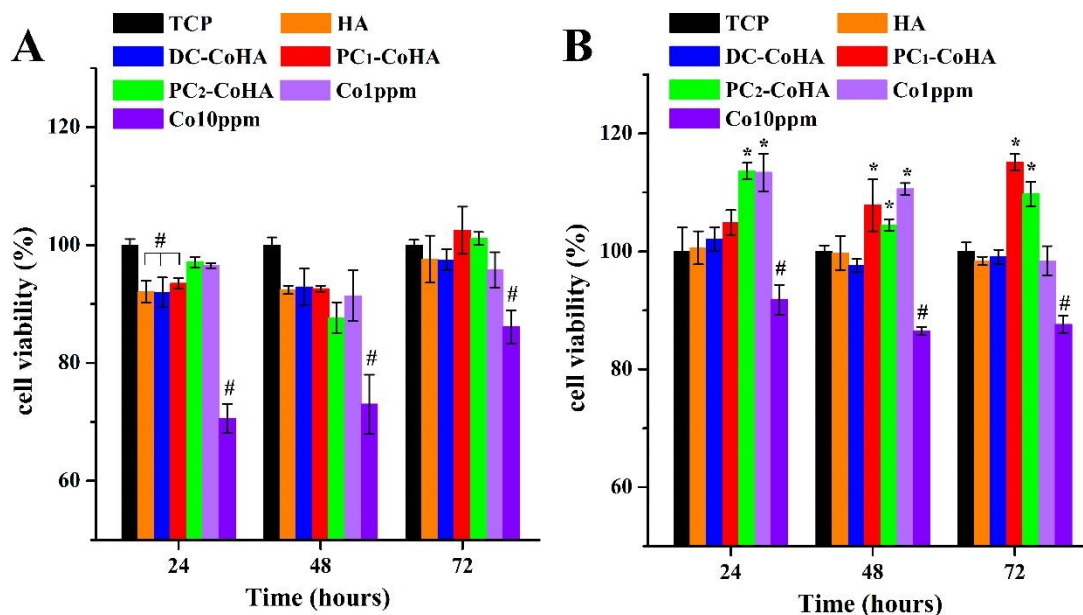


**Figure 9.** CoHA cytotoxicity test using (A) L929 cells and (B) MG63 cells, respectively. \*: Significantly higher than the control group (TCP). #: Significantly lower than the control group ( $p < 0.01$ ).

### 3.8. Extracellular Matrix Mineralization

Calcium deposition is one of the markers for osteoblast growth and differentiation, as well as for osteogenic potential. The MG63 cells were dyed using ARS after culturing in the CoHA extract solution for 7 days. Figure 10 shows the distribution of calcium ion deposition, observed using an optical microscope, which was used for evaluating cell growth and differentiation. The bright red area represents calcium ion deposition. PC<sub>1</sub>-CoHA and PC<sub>2</sub>-CoHA showed more calcium ion depositions on the extracellular matrix. The quantitative analysis results are shown in Figure 10H. After 7 days of culture, cell differentiation for DC-CoHA, PC<sub>1</sub>-CoHA, and PC<sub>2</sub>-CoHA was significantly higher than the other groups, and was 27–31% higher than the TCP control group. The culture of cells using extract solutions with cobalt ion concentrations of 1 ppm and 10 ppm showed that lower cobalt ion concentration could promote MG63 cell growth. A previous study found that cobalt ions can mimic the hypoxic environment and activate HIF-1 $\alpha$  to promote VEGF production [64]. The differentiation of MG63 cells was probably enhanced under the influence of cobalt ions released by CoHA [65–67]. In addition, Nenad Ignjatovic et al. reported that hydrothermal synthesis of CoHA was implanted in the mandible of a rat model of osteoporosis, indicating that the mineral deposition rate of cobalt ion-filled sites is higher than that of pure HA and accelerates the rate of bone formation [15,21]. This is similar to the results of our study, indicating that cobalt ions contribute to the growth and differentiation of bone cells.

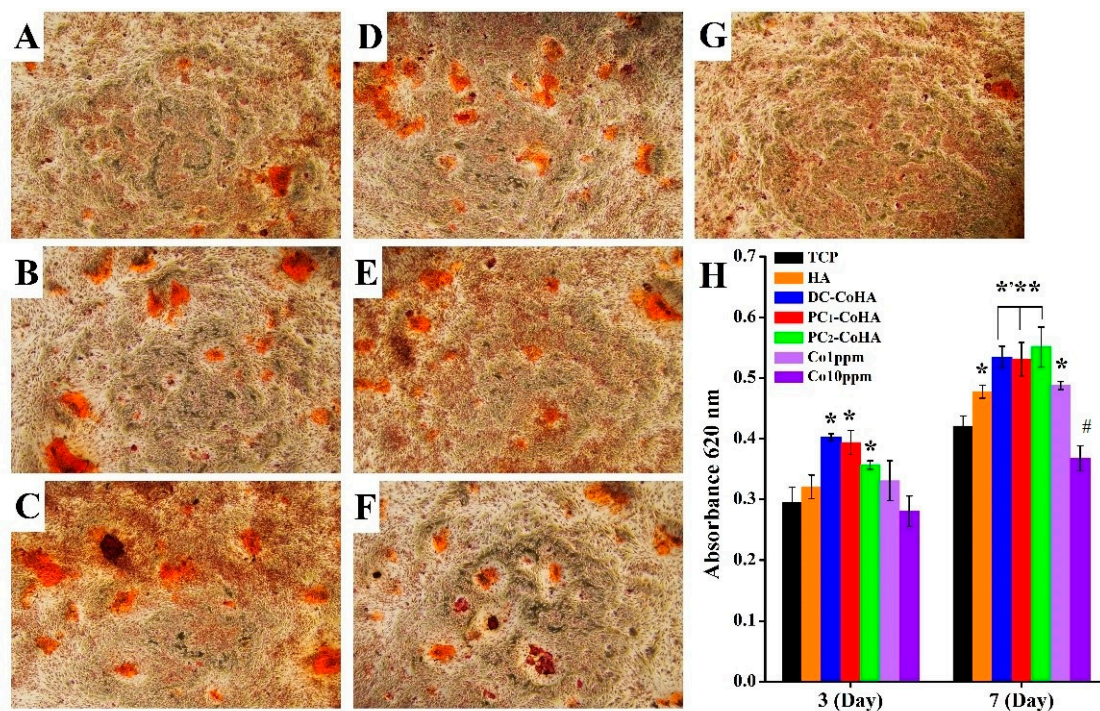


**Figure 10.** The degree of MG63 cells were cultured for 7 days with extracellular matrix mineralization determined by Alizarin Red S (Sigma) staining. (A) tissue culture plate (TCP), (B) HA, (C) DC-CoHA, (D) PC<sub>1</sub>-CoHA (E) PC<sub>2</sub>-CoHA, (F) Co1ppm and (G) Co10ppm. (H) Quantitative analysis of matrix deposition mineralization was performed at 3 and 7 days. \*: Significantly higher than the control group (TCP) \*\*: Significantly higher than HA and Co1ppm groups. #: Significantly lower than the control group ( $p < 0.001$ ).

### 3.9. Antibacterial

The filler material of the bone tissue defect, in addition to helping the growth and differentiation of the bone cells, must also be considered in terms of antibacterial ability. Through the inhibition of bacteria around the bone defect, it reduces the risk of infection to improve the success rate of surgery. In this work, *E. coli* is used as model organism since it is used frequently in antibacterial

experiments. The bacteria was cultured with 6 mg/mL of three CoHA samples for 18 h and then antibacterial evaluation by culturing in BHI agar plates for 24 h and counting the number of colony forming units (CFU) as shown in Figure 11. Results show that all three groups of CoHA have excellent antibacterial activity (Figure 11A–D). Compared with the control group, PC<sub>1</sub>-CoHA (96%) had the highest sterilization rate, followed by DC-CoHA (95%) and PC<sub>2</sub>-CoHA (94%) (Figure 11E). ICP-OES analysis showed that PC<sub>1</sub>-CoHA had the highest release of cobalt ions after soaking in PBS for seven days (Table 3), so it had the best antibacterial ability. This can be explained by the fact that the antibacterial effect mainly comes from the release of cobalt ions. Other literature also reported that cobalt oxide and cobalt ions have good antibacterial performance [68].

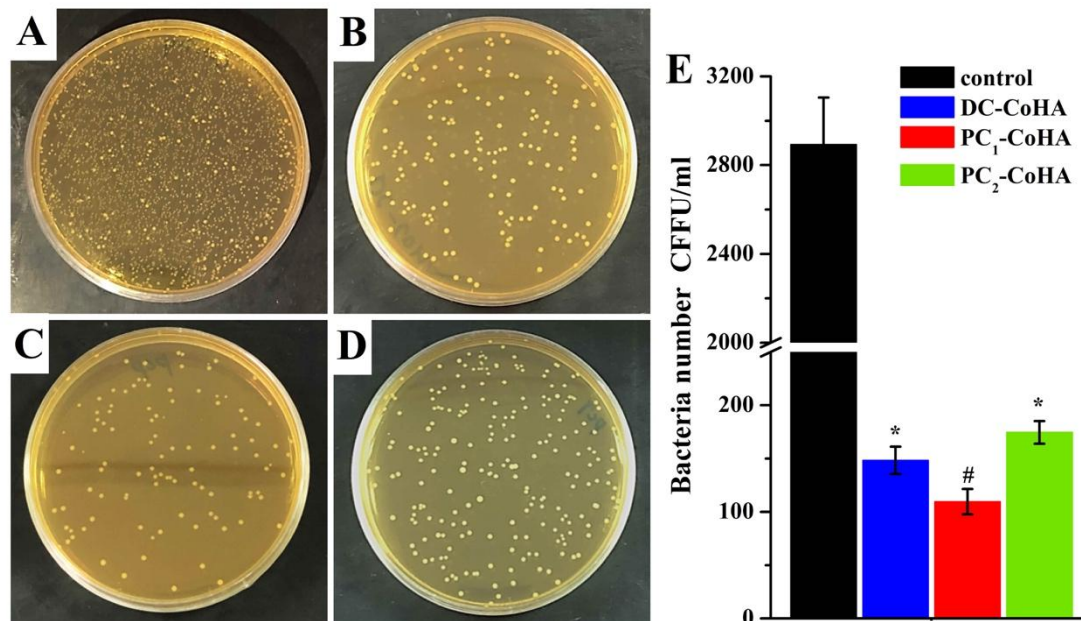


**Figure 11.** Images of the antibacterial results for relatively bacterial colonies on agar plates: (A) control (BHI), (B) DC-CoHA, (C) PC<sub>1</sub>-CoHA and (D) PC<sub>2</sub>-CoHA sample. (E) Antibacterial activity of the analyzed sample on *E. coli*. (\*: significantly smaller than control group. #: significantly smaller than all the other samples,  $p < 0.05$ , mean  $\pm$  standard deviation (SD),  $n = 4$ ).

#### 4. Conclusions

CoHA was successfully prepared using electrochemical deposition and the effects of direct and pulse current supply modes on CoHA were discussed. A more uniform deposition of CoHA was obtained on a titanium surface using pulse electrochemical deposition. Through the direct current power mode, more cobalt ions attach to the surface, while the pulse current mode has higher cobalt ions in the interior. Magnetic analysis results show that more cobalt ions adhere to the surface of CoHA and are of smaller particle size, which will enhance the magnetic properties of the material. CoHA should reduce the inflammatory response of bone tissue after filling due to its free radical scavenging capability. MRI results showed that CoHA had a clear T<sub>2</sub> image at low concentrations, and had a higher relaxation rate than other magnetic nanoparticles reported in literature; thus, it can be used potentially for localization in T<sub>2</sub> imaging. The results of biocompatibility indicate that CoHA promotes the growth and differentiation of bone cells by releasing a small amount of cobalt ions. Furthermore, we emphasize on the application of PC<sub>1</sub>-CoHA as an available and potential bone filling material against *E. coli*. In conclusion, CoHA produced using pulse current has more deposition, higher degradation rate, better bioactivity and antibacterial ability than that produced using direct current. It can improve bone regeneration and induce bone growth, and can be applied in track and localization by MRI. It is expected to be helpful for the development of bone-filled materials.

**Author Contributions:** W.-C.L. and C.-C.C. are the core first authors for contributions to the analysis and interpretation of data, drafting of the manuscript, and critical revision of the manuscript; P.-T.W. carried out the experiment; C.-M.T. was the corresponding author and contributed to the design and implementation of the research, to the analysis of the results and to the writing of the manuscript.

**Funding:** This research was funded by ministry of science and technology of Taiwan, Republic of China, via grants MOST 104-2633-E-040-002.

**Conflicts of Interest:** There are no conflicts to declare.

## References

1. Hu, M.H.; Lee, P.Y.; Chen, W.C.; Hu, J.J. Comparison of three calcium phosphate bone graft substitutes from biomechanical, histological, and crystallographic perspectives using a rat posterolateral lumbar fusion model. *Mater. Sci. Eng. C Mater. Biol. Appl.* **2014**, *45*, 82–88. [[CrossRef](#)] [[PubMed](#)]
2. Hernigou, P.; Dubory, A.; Pariat, J.; Potage, D.; Roubineau, F.; Jammal, S.; Lachaniette, C.F. Beta-tricalcium phosphate for orthopedic reconstructions as an alternative to autogenous bone graft. *Morphologie* **2017**, *101*, 173–179. [[CrossRef](#)] [[PubMed](#)]
3. Hofmann, G.; Kirschner, M.; Wangemann, T.; Falk, C.; Mempel, W.; Hammer, C. Infections and immunological hazards of allogeneic bone transplantation. *Arch. Orthop. Trauma Surg.* **1995**, *114*, 159–166. [[CrossRef](#)] [[PubMed](#)]
4. Zhu, Y.; Zhang, K.; Zhao, R.; Ye, X.; Chen, X.; Xiao, Z.; Yang, X.; Zhu, X.; Zhang, K.; Fan, Y.; et al. Bone regeneration with micro/nano hybrid-structured biphasic calcium phosphate bioceramics at segmental bone defect and the induced immunoregulation of MSCs. *Biomaterials* **2017**, *147*, 133–144. [[CrossRef](#)] [[PubMed](#)]
5. Li, B.; Liu, Z.; Yang, J.; Yi, Z.; Xiao, W.; Liu, X.; Yang, X.; Xu, W.; Liao, X. Preparation of bioactive beta-tricalcium phosphate microspheres as bone graft substitute materials. *Mater. Sci. Eng. C Mater. Biol. Appl.* **2017**, *70*, 1200–1205. [[CrossRef](#)] [[PubMed](#)]
6. Bohner, M.; Galea, L.; Doebelin, N. Calcium phosphate bone graft substitutes: Failures and hopes. *J. Eur. Ceram. Soc.* **2012**, *32*, 2663–2671. [[CrossRef](#)]
7. Kramer, E.R.; Morey, A.M.; Staruch, M.; Suib, S.L.; Jain, M.; Budnick, J.I.; Wei, M. Synthesis and characterization of iron-substituted hydroxyapatite via a simple ion-exchange procedure. *J. Mater. Sci.* **2013**, *48*, 665–673. [[CrossRef](#)]
8. Cox, S.C.; Jamshidi, P.; Grover, L.M.; Mallick, K.K. Preparation and characterisation of nanophase Sr, Mg, and Zn substituted hydroxyapatite by aqueous precipitation. *Mater. Sci. Eng. C* **2014**, *35*, 106–114. [[CrossRef](#)]
9. Stanić, V.; Radosavljević-Mihajlović, A.S.; Živković-Radovanović, V.; Nastasijević, B.; Marinović-Cincović, M.; Marković, J.P.; Budimir, M.D. Synthesis, structural characterisation and antibacterial activity of Ag<sup>+</sup>-doped fluorapatite nanomaterials prepared by neutralization method. *Appl. Surf. Sci.* **2015**, *337*, 72–80. [[CrossRef](#)]
10. Kramer, E.; Itzkowitz, E.; Wei, M. Synthesis and characterization of cobalt-substituted hydroxyapatite powders. *Ceram. Int.* **2014**, *40*, 13471–13480. [[CrossRef](#)]
11. Fan, W.; Crawford, R.; Xiao, Y. Enhancing in vivo vascularized bone formation by cobalt chloride-treated bone marrow stromal cells in a tissue engineered periosteum model. *Biomaterials* **2010**, *31*, 3580–3589. [[CrossRef](#)] [[PubMed](#)]
12. Zhou, J.; Zhao, L. Hypoxia-mimicking Co doped TiO<sub>2</sub> microporous coating on titanium with enhanced angiogenic and osteogenic activities. *Acta Biomater.* **2016**, *43*, 358–368. [[CrossRef](#)]
13. Kulanthaivel, S.; Mishra, U.; Agarwal, T.; Giri, S.; Pal, K.; Pramanik, K.; Banerjee, I. Improving the osteogenic and angiogenic properties of synthetic hydroxyapatite by dual doping of bivalent cobalt and magnesium ion. *Ceram. Int.* **2015**, *41*, 11323–11333. [[CrossRef](#)]
14. Tahmasebi Birgani, Z.; Fennema, E.; Gijbels, M.J.; de Boer, J.; van Blitterswijk, C.A.; Habibovic, P. Stimulatory effect of cobalt ions incorporated into calcium phosphate coatings on neovascularization in an in vivo intramuscular model in goats. *Acta Biomater.* **2016**, *36*, 267–276. [[CrossRef](#)] [[PubMed](#)]
15. Ignjatovic, N.; Ajdukovic, Z.; Rajkovic, J.; Najman, S.; Mihailovic, D.; Uskokovic, D. Enhanced Osteogenesis of nanosized cobalt-substituted hydroxyapatite. *J. Bionic Eng.* **2015**, *12*, 604–612. [[CrossRef](#)]
16. Sarath Chandra, V.; Elayaraja, K.; Thanigai Arul, K.; Ferraris, S.; Spriano, S.; Ferraris, M.; Asokan, K.; Narayana Kalkura, S. Synthesis of magnetic hydroxyapatite by hydrothermal–microwave technique: Dielectric, protein adsorption, blood compatibility and drug release studies. *Ceram. Int.* **2015**, *41*, 13153–13163. [[CrossRef](#)]

17. Wang, G.; Ma, Y.; Wei, Z.; Qi, M. Development of multifunctional cobalt ferrite/graphene oxide nanocomposites for magnetic resonance imaging and controlled drug delivery. *Chem. Eng. J.* **2016**, *289*, 150–160. [[CrossRef](#)]
18. Shokrollahi, H. Contrast agents for MRI. *Mater. Sci. Eng. C* **2013**, *33*, 4485–4497. [[CrossRef](#)]
19. Stojanović, Z.; Veselinović, L.; Marković, S.; Ignjatović, N.; Uskoković, D. Hydrothermal synthesis of nanosized pure and cobalt-exchanged hydroxyapatite. *Mater. Manuf. Process.* **2009**, *24*, 1096–1103. [[CrossRef](#)]
20. Veselinović, L.; Karanović, L.; Stojanović, Z.; Bračko, I.; Marković, S.; Ignjatović, N.; Uskoković, D. Crystal structure of cobalt-substituted calcium hydroxyapatite nanopowders prepared by hydrothermal processing. *J. Appl. Crystallogr.* **2010**, *43*, 320–327. [[CrossRef](#)]
21. Ignjatović, N.; Ajduković, Z.; Savić, V.; Najman, S.; Mihailović, D.; Vasiljević, P.; Stojanović, Z.; Uskoković, V.; Uskoković, D. Nanoparticles of cobalt-substituted hydroxyapatite in regeneration of mandibular osteoporotic bones. *J. Mater. Sci. Mater. Med.* **2013**, *24*, 343–354. [[CrossRef](#)] [[PubMed](#)]
22. Kothapalli, C.; Wei, M.; Vasiliev, A.; Shaw, M. Influence of temperature and concentration on the sintering behavior and mechanical properties of hydroxyapatite. *Acta Mater.* **2004**, *52*, 5655–5663. [[CrossRef](#)]
23. Isa, N.N.C.; Mohd, Y.; Yury, N. Electrochemical Deposition and Characterization of Hydroxyapatite (HAp) on Titanium Substrate. *APCBEE Procedia* **2012**, *3*, 46–52. [[CrossRef](#)]
24. Yousefpour, M.; Afshar, A.; Yang, X.; Li, X.; Yang, B.; Wu, Y.; Chen, J.; Zhang, X. Nano-crystalline growth of electrochemically deposited apatite coating on pure titanium. *J. Electroanal. Chem.* **2006**, *589*, 96–105. [[CrossRef](#)]
25. Parcharoen, Y.; Kajitvichyanukul, P.; Sirivisoot, S.; Termsuksawad, P. Hydroxyapatite electrodeposition on anodized titanium nanotubes for orthopedic applications. *Appl. Surf. Sci.* **2014**, *311*, 54–61. [[CrossRef](#)]
26. Park, J.-H.; Lee, D.-Y.; Oh, K.-T.; Lee, Y.-K.; Kim, K.-M.; Kim, K.-N. Bioactivity of calcium phosphate coatings prepared by electrodeposition in a modified simulated body fluid. *Mater. Lett.* **2006**, *60*, 2573–2577. [[CrossRef](#)]
27. Hayakawa, T.; Kawashita, M.; Takaoaka, G.H. Coating of hydroxyapatite films on titanium substrates by electrodeposition under pulse current. *J. Ceram. Soc. Jpn.* **2008**, *116*, 68–73. [[CrossRef](#)]
28. Manso, M.; Jimenez, C.; Morant, C.; Herrero, P.; Martinez-Duart, J. Electrodeposition of hydroxyapatite coatings in basic conditions. *Biomaterials* **2000**, *21*, 1755–1761. [[CrossRef](#)]
29. Park, J.-H.; Lee, D.-Y.; Oh, K.-T.; Lec, Y.; Kim, K.-N. Bioactive calcium phosphate coating on sodium hydroxide-pretreated titanium substrate by electrodeposition. *J. Am. Ceram. Soc.* **2004**, *87*, 1792–1794. [[CrossRef](#)]
30. Dumelie, N.; Benhayoune, H.; Richard, D.; Laurent-Maquin, D.; Balossier, G. In vitro precipitation of electrodeposited calcium-deficient hydroxyapatite coatings on Ti6Al4V substrate. *Mater. Charact.* **2008**, *59*, 129–133. [[CrossRef](#)]
31. Lee, K.; Jeong, Y.-H.; Ko, Y.-M.; Choe, H.-C.; Brantley, W.A. Hydroxyapatite coating on micropore-formed titanium alloy utilizing electrochemical deposition. *Thin Solid Films* **2013**, *549*, 154–158. [[CrossRef](#)]
32. Marashi-Najafi, F.; Khalil-Allafi, J.; Etmianfar, M.R. Biocompatibility of hydroxyapatite coatings deposited by pulse electrodeposition technique on the Nitinol superelastic alloy. *Mater. Sci. Eng. C Mater. Biol. Appl.* **2017**, *76*, 278–286. [[CrossRef](#)] [[PubMed](#)]
33. Lin, W.-C.; Yan, M.; Tang, C.-M. Effect of the electrolyte composition of cobalt substituted hydroxyapatite by electrodeposition process. In Proceedings of the 15th Asian Bioceramics Symposium (ABC2015), Tokyo, Japan, 9–11 December 2015.
34. He, C.; Xiao, G.; Jin, X.; Sun, C.; Ma, P.X. Electrodeposition on nanofibrous polymer scaffolds: Rapid mineralization, tunable calcium phosphate composition and topography. *Adv. Funct. Mater.* **2010**, *20*, 3568–3576. [[CrossRef](#)] [[PubMed](#)]
35. Gopi, D.; Indira, J.; Kavitha, L.; Kannan, S.; Ferreira, J. Spectroscopic characterization of nanohydroxyapatite synthesized by molten salt method. *Spectrochim. Acta Part A Mol. Biomol. Spectrosc.* **2010**, *77*, 545–547. [[CrossRef](#)]
36. Brand-Williams, W.; Cuvelier, M.-E.; Berset, C. Use of a free radical method to evaluate antioxidant activity. *LWT-Food Sci. Technol.* **1995**, *28*, 25–30. [[CrossRef](#)]
37. Tang, C.-M.; Tian, Y.-H.; Hsu, S.-H. Poly(vinyl alcohol) Nanocomposites Reinforced with Bamboo Charcoal Nanoparticles: Mineralization Behavior and Characterization. *Materials* **2015**, *8*, 4895–4911. [[CrossRef](#)] [[PubMed](#)]



38. Joshi, H.M.; Lin, Y.P.; Aslam, M.; Prasad, P.; Schultz-Sikma, E.A.; Edelman, R.; Meade, T.; Dravid, V.P. Effects of shape and size of cobalt ferrite nanostructures on their MRI contrast and thermal activation. *J. Phys. Chem. C* **2009**, *113*, 17761–17767. [[CrossRef](#)] [[PubMed](#)]
39. Gopi, D.; Karthika, A.; Nithiya, S.; Kavitha, L. In vitro biological performance of minerals substituted hydroxyapatite coating by pulsed electrodeposition method. *Mater. Chem. Phys.* **2014**, *144*, 75–85. [[CrossRef](#)]
40. Utku, F.S.; Seckin, E.; Goller, G.; Tamerler, C.; Urgen, M. Carbonated hydroxyapatite deposition at physiological temperature on ordered titanium oxide nanotubes using pulsed electrochemistry. *Ceram. Int.* **2014**, *40*, 15479–15487. [[CrossRef](#)]
41. Kolmas, J.; Piotrowska, U.; Kuras, M.; Kurek, E. Effect of carbonate substitution on physicochemical and biological properties of silver containing hydroxyapatites. *Mater. Sci. Eng. C Mater. Biol. Appl.* **2017**, *74*, 124–130. [[CrossRef](#)]
42. Sønju Clasen, A.; Ruyter, I. Quantitative determination of type A and type B carbonate in human deciduous and permanent enamel by means of Fourier transform infrared spectrometry. *Adv. Dent. Res.* **1997**, *11*, 523–527. [[CrossRef](#)] [[PubMed](#)]
43. Ortali, C.; Julien, I.; Vandenhende, M.; Drouet, C.; Champion, E. Consolidation of bone-like apatite bioceramics by spark plasma sintering of amorphous carbonated calcium phosphate at very low temperature. *J. Eur. Ceram. Soc.* **2018**, *38*, 2098–2109. [[CrossRef](#)]
44. Ishikawa, K. Bone Substitute Fabrication Based on Dissolution-Precipitation Reactions. *Materials* **2010**, *3*, 1138–1155. [[CrossRef](#)]
45. Gopi, D.; Indira, J.; Kavitha, L.; Sekar, M.; Mudali, U.K. Synthesis of hydroxyapatite nanoparticles by a novel ultrasonic assisted with mixed hollow sphere template method. *Spectrochim. Acta Part A Mol. Biomol. Spectrosc.* **2012**, *93*, 131–134. [[CrossRef](#)] [[PubMed](#)]
46. Mabilieu, G.; Filmon, R.; Petrov, P.; Baslé, M.; Sabokbar, A.; Chappard, D. Cobalt, chromium and nickel affect hydroxyapatite crystal growth in vitro. *Acta Biomater.* **2010**, *6*, 1555–1560. [[CrossRef](#)] [[PubMed](#)]
47. Li, J.; Chen, Y.; Yin, Y.; Yao, F.; Yao, K. Modulation of nano-hydroxyapatite size via formation on chitosan–gelatin network film in situ. *Biomaterials* **2007**, *28*, 781–790. [[CrossRef](#)]
48. Ding, M.; Xi, J.; Ji, Z. Size-controlled synthesis, growth mechanism and magnetic properties of cobalt microspheres. *Mater. Lett.* **2017**, *201*, 27–30. [[CrossRef](#)]
49. Wang, Y.; Yang, X.; Gu, Z.; Qin, H.; Li, L.; Liu, J.; Yu, X. In vitro study on the degradation of lithium-doped hydroxyapatite for bone tissue engineering scaffold. *Mater. Sci. Eng. C Mater. Biol. Appl.* **2016**, *66*, 185–192. [[CrossRef](#)]
50. Chen, Z.; Du, Y.; Li, Z.; Yang, K.; Lv, X. Controllable synthesis of magnetic Fe<sub>3</sub>O<sub>4</sub> particles with different morphology by one-step hydrothermal route. *J. Magn. Magn. Mater.* **2017**, *426*, 121–125. [[CrossRef](#)]
51. Sumathi, S.; Gopal, B. In vitro degradation of multisubstituted hydroxyapatite and fluorapatite in the physiological condition. *J. Cryst. Growth* **2015**, *422*, 36–43. [[CrossRef](#)]
52. Kheradmandfard, M.; Fathi, M.H.; Ahangarian, M.; Zahrani, E.M. In vitro bioactivity evaluation of magnesium-substituted fluorapatite nanopowders. *Ceram. Int.* **2012**, *38*, 169–175. [[CrossRef](#)]
53. Hsu, S.-h.; Tang, C.-M.; Tseng, H.-J. Gold nanoparticles induce surface morphological transformation in polyurethane and affect the cellular response. *Biomacromolecules* **2007**, *9*, 241–248. [[CrossRef](#)] [[PubMed](#)]
54. Lin, M.M.; Kim, D.K.; El Haj, A.J.; Dobson, J. Development of superparamagnetic iron oxide nanoparticles (SPIONS) for translation to clinical applications. *IEEE Trans. Nanobiosci.* **2008**, *7*, 298–305.
55. Gupta, A.K.; Gupta, M. Synthesis and surface engineering of iron oxide nanoparticles for biomedical applications. *Biomaterials* **2005**, *26*, 3995–4021. [[CrossRef](#)]
56. Bowers, M.E.; Tung, G.A.; Trinh, N.; Leventhal, E.; Crisco, J.J.; Kimia, B.; Fleming, B.C. Effects of ACL interference screws on articular cartilage volume and thickness measurements with 1.5 T and 3 T MRI. *Osteoarthr. Cartil.* **2008**, *16*, 572–578. [[CrossRef](#)] [[PubMed](#)]
57. Jun, Y.W.; Lee, J.H.; Cheon, J. Chemical design of nanoparticle probes for high-performance magnetic resonance imaging. *Angew. Chem. Int. Ed. Engl.* **2008**, *47*, 5122–5135. [[CrossRef](#)]
58. Wu, H.; Liu, G.; Wang, X.; Zhang, J.; Chen, Y.; Shi, J.; Yang, H.; Hu, H.; Yang, S. Solvothermal synthesis of cobalt ferrite nanoparticles loaded on multiwalled carbon nanotubes for magnetic resonance imaging and drug delivery. *Acta Biomater.* **2011**, *7*, 3496–3504. [[CrossRef](#)]

59. Parkes, L.M.; Hodgson, R.; Lu le, T.; Tung le, D.; Robinson, I.; Fernig, D.G.; Thanh, N.T. Cobalt nanoparticles as a novel magnetic resonance contrast agent—relaxivities at 1.5 and 3 Tesla. *Contrast Media Mol. Imaging* **2008**, *3*, 150–156. [[CrossRef](#)]
60. Jun, Y.-W.; Huh, Y.-M.; Choi, J.-S.; Lee, J.-H.; Song, H.-T.; Kim, S.; Kim, S.; Yoon, S.; Kim, K.-S.; Shin, J.-S. Nanoscale size effect of magnetic nanocrystals and their utilization for cancer diagnosis via magnetic resonance imaging. *J. Am. Chem. Soc.* **2005**, *127*, 5732–5733. [[CrossRef](#)]
61. Tanaka, O.; Nishigaki, Y.; Hayashi, H.; Iida, T.; Yokoyama, T.; Takenaka, E.; Yama, E.; Tomita, E. The advantage of iron-containing fiducial markers placed with a thin needle for radiotherapy of liver cancer in terms of visualization on MRI: An initial experience of Gold Anchor. *Radiol. Case Rep.* **2017**, *12*, 416–421. [[CrossRef](#)]
62. Hossain, M.; Schirmer, T.; Richardson, T.; Chen, L.; Buyyounouski, M.K.; Ma, C.M. Effect of gold marker seeds on magnetic resonance spectroscopy of the prostate. *Int. J. Radiat. Oncol. Biol. Phys.* **2012**, *83*, 451–458. [[CrossRef](#)] [[PubMed](#)]
63. Shakir, S.I.; Udrescu, C.; Enachescu, C.; Rouviere, O.; Arion, S.; Caraivan, I.; Chapet, O. Transrectal implantation and stability of gold markers in prostate bed for salvage radiotherapy of macroscopic recurrences. *Phys. Med.* **2016**, *32*, 1422–1427. [[CrossRef](#)] [[PubMed](#)]
64. Loboda, A.; Jazwa, A.; Wegiel, B.; Jozkowicz, A.; Dulak, J. Heme oxygenase-1-dependent and-independent regulation of angiogenic genes expression: Effect of cobalt protoporphyrin and cobalt chloride on VEGF and IL-8 synthesis in human microvascular endothelial cells. *Cell. Mol. Boil.* **2005**, *51*, 347.
65. Wu, C.; Zhou, Y.; Fan, W.; Han, P.; Chang, J.; Yuen, J.; Zhang, M.; Xiao, Y. Hypoxia-mimicking mesoporous bioactive glass scaffolds with controllable cobalt ion release for bone tissue engineering. *Biomaterials* **2012**, *33*, 2076–2085. [[CrossRef](#)] [[PubMed](#)]
66. Quinlan, E.; Partap, S.; Azevedo, M.M.; Jell, G.; Stevens, M.M.; O'Brien, F.J. Hypoxia-mimicking bioactive glass/collagen glycosaminoglycan composite scaffolds to enhance angiogenesis and bone repair. *Biomaterials* **2015**, *52*, 358–366. [[CrossRef](#)] [[PubMed](#)]
67. Chen, Z.; Yuen, J.; Crawford, R.; Chang, J.; Wu, C.; Xiao, Y. The effect of osteoimmunomodulation on the osteogenic effects of cobalt incorporated beta-tricalcium phosphate. *Biomaterials* **2015**, *61*, 126–138. [[CrossRef](#)] [[PubMed](#)]
68. Kavitha, T.; Haider, S.; Kamal, T.; Ul-Islam, M. Thermal decomposition of metal complex precursor as route to the synthesis of Co<sub>3</sub>O<sub>4</sub> nanoparticles: Antibacterial activity and mechanism. *J. Alloy Compd.* **2017**, *704*, 296–302. [[CrossRef](#)]



© 2018 by the authors. Licensee MDPI, Basel, Switzerland. This article is an open access article distributed under the terms and conditions of the Creative Commons Attribution (CC BY) license (<http://creativecommons.org/licenses/by/4.0/>).